A Novel Turbomachinery Air-Brake Concept for Quiet Aircraft

P. N. Shah
e-mail: parthiv@alum.mit.edu

D. D. Mobed
e-mail: dmobed@alum.mit.edu

Z. S. Spakovszky
e-mail: zolti@mit.edu

MIT Gas Turbine Laboratory,
Massachusetts Institute of Technology,
Cambridge, MA 02139

A novel air-brake concept for next-generation, low-noise civil aircraft is introduced. Deployment of such devices in clean airframe configuration can potentially reduce aircraft source noise and noise propagation to the ground. The generation of swirling outflow from a duct, such as an aircraft engine, is demonstrated to have high drag and low noise. The simplest configuration is a ram pressure-driven duct with stationary swirl vanes, a so-called swirl tube. A detailed aerodynamic design is performed using first principles based modeling and high-fidelity numerical simulations. The swirl-drag-noise relationship is quantified through scale-model aerodynamic and aeroacoustic wind tunnel tests. The maximum measured stable flow drag coefficient is 0.83 at exit swirl angles close to 50 deg. The acoustic signature, extrapolated to full-scale, is found to be well below the background noise of a well-populated area. Vortex breakdown is found to be the aerodynamically and acoustically limiting phenomenon, generating a white-noise signature that is about 15 dB louder than a stable swirling flow.
[DOI: 10.1115/1.3192145]

1 Introduction and Background

Airframe noise depends on an aircraft's aerodynamic configuration, approach speed, and flight path angle. For modern and next-generation, large civil aircraft on approach, Lilley [1] showed that airframe noise competes with engine noise, due to the significant achievements made in engine noise reduction from high bypass ratio engine cycles. Drastic noise reduction in engine sources through ultra-high bypass ratios (greater than 15), and mitigation of airframe sources through clean, all-lifting planforms still leaves self-noise associated with the clean airframe. This self-noise is referred to as the ultimate noise barrier [2], and sets an upper limit to further airframe source noise reduction.

Clean airframe noise scales with the fifth power of velocity, due to the scattering of acoustic energy from turbulent boundary layer eddies passing the airframe trailing edge [3], and scales as the square of the distance due to spherical spreading of the acoustic wavefronts, i.e.,

$$\text{noise reduction (dB)} = 10 \log_{10}\left(\frac{V}{V_{\text{ref}}}\right)^5 \left(\frac{r_{\text{ref}}}{r}\right)^2 \tag{1}$$

This scaling law suggests that the operational shift to slower and steeper flight with clean aerodynamics is a means to reduce the community noise footprint [4]. Operational changes such as continuous descent approaches (CDAs) have achieved significant reductions in community noise exposure by keeping the aircraft higher and at lower thrust, eliminating level flight segments and associated thrust transients [5,6]. Displaced threshold landings have also been recommended for noise abatement [4], though their feasibility is airport dependent. Recent certification efforts of the Airbus A318 for 5.5 deg glideslope approaches at London City Airport indicate that steeper flight has the additional benefit of access to greater numbers of small airports in confined settings [7].

Recently, the Cambridge-MIT Institute (CMI) silent aircraft initiative (SAI) has developed a novel conceptual aircraft design

with noise as a primary design variable [8–11]. The conceptual design, called the Silent Aircraft eXperimental design (SAX), combines technological improvements such as acoustically shielded [12], ultra-high bypass ratio engines [13] and cleaner aerodynamics with operational measures such as slower and steeper approach profiles. Design for such an operational change introduces the requirement for additional quiet drag, to compensate for the loss of drag from the absence of conventional high-lift devices and fairing of landing gear. Quiet drag devices would effectively serve as air-brakes that may allow an aircraft to fly a desired approach profile. For example, a quiet drag coefficient of about 1 based on total aircraft propulsion system fan area is suggested to enable a glideslope increase from 3 deg to 4 deg at constant speed, resulting in a potential overall noise reduction of 2.5 dB [14,15].

1.1 Nature of the Issues. A key challenge to realizing quiet drag is that conventional high-drag devices such as flaps and slats may have a strong correlation between drag and noise, as suggested by Smith [2] (p. 45). The same may be true for landing gear. When source noise is reduced by cleaning up the airframe aerodynamics, i.e., by suppressing the unsteady flow structures from these conventional drag devices, drag is also inherently reduced. The key difference of a quiet drag device, then, is a departure from this correlation.

A novel device to address this challenge is introduced with the hypothesis that a swirling exhaust flow (for example, the jet engine exhaust) generates a streamwise vortex, which is in essence quiet. The swirling motion yields low pressure in the vortex core and therefore pressure drag. This research demonstrates that a drag coefficient of about 0.8, based on through-flow area, can be achieved with a quiet far-field noise signature of about 44 dBA at full-scale. One conceptual implementation of such a device is the use of variable outlet guide vanes (OGVs) in a turbofan bypass duct, as shown in Fig. 1(a).

To assess the idea, the simplest configuration is conceived as a ram pressure-driven or throttled device without moving parts. This device is referred to as a swirl tube, and is depicted in Fig. 1(b). The ram pressure-driven swirl tube is the focus of detailed analysis, design, and experimentation. ram pressure-driven swirling exhaust flows are markedly different from a swirling jet. In addition to swirl, this flow has a jetlike axial velocity on the centerline,
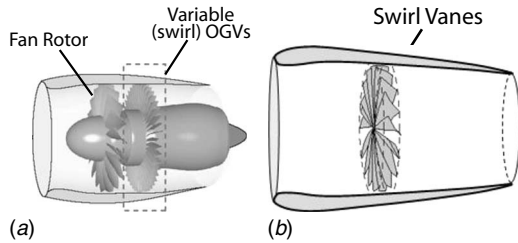
Fig. 1 Quiet air-brake concepts: (a) fan-driven or pumped configuration and (b) ram pressure-driven configuration, a so-called swirl tube
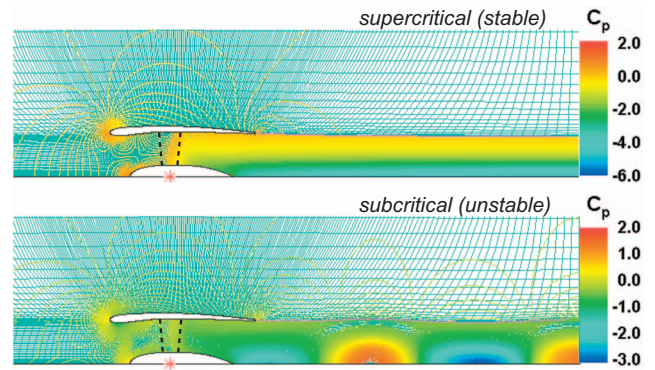

Fig. 2 Isocontours of pressure coefficient at super- and subcritical swirl levels. Vortex breakdown instability numerically indicated by waves on vortex core (for illustration purposes the contour density is increased for the swirling exhaust flow).

relative to the freestream, and a wakelike axial velocity near the duct outer radius. A number of researchers have investigated the fluid dynamics of swirling jets and/or wakes [16,17] and, to a lesser extent, swirling jet acoustics [18,19]. To the authors' knowledge, however, the fluid dynamics and acoustics of swirling wake flows have not received consideration in the context of through-flow devices for the purpose of drag generation.

A key limitation of swirling flows is the onset of vortex breakdown. A large amount of research has been conducted on the vortex breakdown phenomenon, and is summarized in seminal reviews [20–22]. The effect of the vortex breakdown instability on the aerodynamics and acoustic performance of such drag generating flows is the new aspect addressed here. Major unknowns are the acoustic signature and the stability limit of swirling exhaust flows, which need to be quantified. The hypothesized sources include acoustic scattering of turbulent structures past trailing edges (e.g., duct exit), vane wake self-noise, quadrupole sources associated with the turbulent structures in the swirling outflow, and noise from vortex breakdown in the vicinity of the duct exit.

1.2 Scope of the Paper. The research presented here focuses mainly on the aerodynamics, and provides an overview of the acoustics of a novel air-brake concept. More details on the acoustics may be found in [23].

The goals of the research effort are to (1) establish and quantify, in a rigorous way, the relationship between swirl, drag, and noise; (2) assess the stability limit, define a criterion for vortex breakdown, and determine its implications on drag and noise; and (3) dissect and quantify the acoustic signature of swirling exhaust flows. The technical approach combines analytical modeling and computational design at different levels of fidelity with experimental assessment of the aerodynamic and acoustic behavior.

2 Swirling Flow Concepts

All swirling flows are vortical structures that originate in the boundary layers of the surfaces over which the working fluid moves. In the case of the swirl tube, the vortex lines are generated in the boundary layers of swirl vanes and the internal nacelle endwalls. Aft of the vanes these lines become aligned with the bulk fluid motion so as to develop a strong streamwise component of vorticity at the duct exit.

For inviscid flows with negligible radial velocity, the simple radial equilibrium equation illustrates that highly swirling flows may sustain strong radial pressure gradients,

$$\frac{\partial p}{\partial r} = \frac{\rho V_\theta^2}{r} \qquad (2)$$

In addition, the axial and the circumferential velocity fields are strongly coupled, as energy conservation in the absence of lost work constrains the balance of kinetic energy components $u_x^2/2$ and $u_\theta^2/2$, and flow work, p/ρ. The strong coupling means that the vortex core becomes increasingly sensitive to far-field variations in pressure. Because of this sensitivity, the natural stability limit of many classes of swirling flows is vortex breakdown, manifested

as an abrupt change in flow properties. At high Reynolds number this includes unsteadiness, turbulence, and rapid diffusion of primary vorticity.

The concept of critical state is adopted here to describe the onset of vortex breakdown. An in-depth review is given by Hall [21]. Using wave theory, Squire [24] and Benjamin [25] developed an eigenvalue problem that admits standing wave solutions at swirl levels beyond a critical value. Darmofal et al. [26] suggested that vortex breakdown is a transition from a super- to a subcritical flow state, where a disturbance propagation speed equals a convective speed, analogous to a hydraulic jump or a one-dimensional shock wave in a compressible fluid. In steady numerical calculations, this can lead to unconverged solutions and the possible admittance of wavelike behavior along the vortex core. This is illustrated by axisymmetric streamline curvature computations in the supercritical (stable) and subcritical (unstable) regimes shown in Fig. 2.

Many naturally occurring vortices are well represented by a Burger vortex circulation distribution. Hence, this distribution is the adopted design choice for the swirl tube. It is defined by the maximum circulation and the critical radius, K_c^* and r_{crit}^*, respectively,

$$\frac{rV_{\theta,d}}{r_d V_\infty} = K_c^* \left[1 - \exp\left(-1.26 \frac{r^{*2}}{r_{crit}^{*2}} \right) \right] \qquad (3)$$

The radial coordinate is nondimensionalized by the duct exhaust radius, r_d, e.g., $r^* = r/r_d$. This circulation distribution approaches a forced vortex on the centerline, and a free vortex at the outer radius [27]. The transition from forced to free vortex may be thought of as occurring at r_{crit}^*. Delery [20] suggested that the salient feature of axisymmetric swirling flows near the breakdown threshold is a swirl parameter, S_D, of 1.2, defined as

$$S_D = \frac{\Gamma_0}{V_\infty r_c} \qquad (4)$$

where r_c is the vortex core radius and $\Gamma_0 = r_c V_{\theta,c}$ is the circulation around a circle of radius r_c. The critical value of $S_D = 1.2$ is generally accepted as the threshold value and is in agreement with other theoretical approaches. The corresponding maximum flow angle is near 50 deg. Here, we simplify the swirl parameter, S, for the onset of vortex breakdown,

$$S = (S_D)_{r_c = r_{crit}} = \left(\frac{V_\theta}{V_x} \right)_{r_c = r_{crit}} \qquad (5)$$

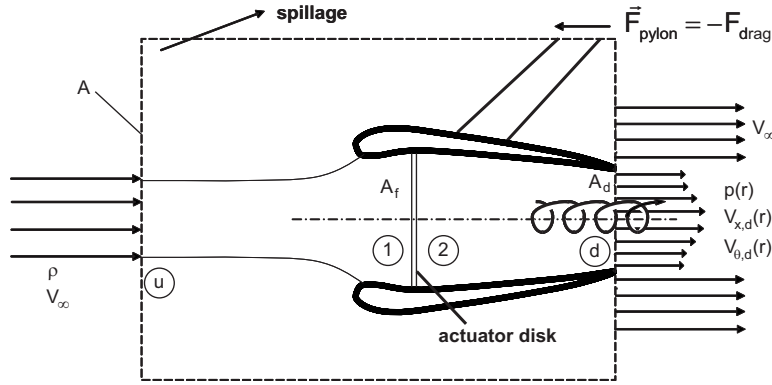It will be shown that this criterion is a valid indicator of the flow regime transition to vortex breakdown.

Fig. 3 Control volume analysis of swirling exhaust flow for drag generation

3 Aerodynamic Design

The aerodynamic design is carried out at three levels of fidelity. The first step is a first principles control volume analysis that defines the parameter space for a higher fidelity assessment of the swirl tube, and establishes bounds on the drag capabilities of different device concepts. This analysis also demonstrates that higher drag coefficients can be achieved with swirl, as compared with purely axial exhaust flows. This is followed by axisymmetric streamline curvature calculations on a nacelle with an internal actuator disk that imparts loss and swirl, to scope the design space and determine vane exit angle settings for a family of swirl tubes that span a range of drag coefficients. This permits three-dimensional vane design. Finally, single passage periodic, Reynolds averaged Navier–Stokes (RANS) computational fluid dynamics (CFD) simulations of the different swirl tube external and internal flow fields are performed to assess the exit flow fields and to predict the onset of vortex breakdown and the drag coefficient.

3.1 Control Volume Analysis. Figure 3 depicts a control volume of cross-sectional area A drawn around a ram air-driven duct containing an internal actuator disk that imparts a discontinuous change in swirl and total pressure distribution as a function of radius. Flow is assumed to be steady and incompressible. The actuator disk area is A_f, while the duct exit, or discharge area, is A_d. For simplicity we consider the case where $A_f = A_d$. Further assumptions in this analysis are as follows: (1) The exit flow at station d satisfies simple radial equilibrium, (2) there is uniform axial flow at stations u and 1, (3) freestream flow that is diverted (spilled) around the duct remains attached, and near the duct trailing edge the external flow returns to freestream velocity and direction, and (4) the upper and lower boundaries are sufficiently far away from the device such that the streamlines are nearly parallel to the freestream flow.[1]

The outcome of the analysis is an expression for the drag coefficient, normalized to the actuator disk area, that depends on the net axial momentum flux and a pressure drag term

$$C_D = \frac{F_{\text{drag}}}{\frac{1}{2}\rho_\infty V_\infty^2 A_f} = \frac{1}{A_f}\int_{A_d}\left[\underbrace{2\frac{V_{x,d}(r)}{V_\infty}\left(1 - \frac{V_{x,d}(r)}{V_\infty}\right)}_{\text{axial momentum flux defect}} - \underbrace{C_p(r)}_{\text{pressure drag}}\right]dA \tag{6}$$

For steady, nonswirling exhaust flows, the duct exit streamlines are straight and parallel, eliminating the pressure drag term. The integrand of the axial momentum flux term is maximum for axial exit velocity ratios,[2] $V_{x,d}/V_\infty$, of 0.5, yielding a maximum drag

---

[1]This allows for some flow with small but finite radial velocity component to spill or entrain both mass and axial momentum across the outer control volume boundary.

[2]For uniform axial exhaust flows, literature on base flows with bleed [28,29] suggests that the control volume model is valid for velocity ratios above 0.25. Below this velocity ratio vortex shedding occurs.

coefficient of 0.5. The two competing effects of actuator disk pressure drop and nacelle lip suction forces due to flow spillage (see [27]) determine the maximum value of C_D, as discussed in [14]. It will be shown that swirling flow can nearly double the drag coefficient relative to nonswirling exhaust flows.

By defining the circulation distribution (rV_θ) and the total pressure loss coefficient at the duct exit, $\bar{\omega}$, an explicit expression for the drag can be obtained as

$$C_D = \frac{1}{A_f}\int_A\left[2\sqrt{1 - \bar{\omega}(r^*) - \left(\frac{V_{\theta,d}}{V_\infty}\right)^2 + \int_{r^*}^1\frac{2(V_{\theta,d}/V_\infty)^2}{\tilde{r}}d\tilde{r}}\right.$$
$$\times\left.\left(1 - \sqrt{1 - \bar{\omega}(r^*) - \left(\frac{V_{\theta,d}}{V_\infty}\right)^2 + \int_{r^*}^1\frac{2(V_{\theta,d}/V_\infty)^2}{\tilde{r}}d\tilde{r}}\right)\right]dA$$
$$+ \frac{1}{A_f}\int_A\int_{r^*}^1\frac{2(V_{\theta,d}/V_\infty)^2}{\tilde{r}}d\tilde{r}dA = C_{D,\text{ax.mom.}} + C_{D,\text{press}} \tag{7}$$

For a detailed derivation, see [14].

Figure 4(a) presents isocontours of drag coefficient overlayed by isocontours of swirl parameter in the design space defined by the dimensionless Burger vortex parameters K_c^* and r_{crit}^*. A loss coefficient normalized to freestream dynamic pressure of $\bar{\omega} = 0.08$ across the actuator disk was assumed, typical of turbomachinery. At the duct exit outer radius, energy conservation constrains the sum of the axial and circumferential components of the dynamic pressure. The maximum swirl multiplier for a given critical radius is limited to the value that corresponds to stagnated flow, i.e., $V_{x,d} = 0$, at the duct exit outer radius[3]

$$(K_c^*)_{\max} = \frac{\sqrt{1 + \bar{\omega}}}{1 - \exp\left[\frac{-1.26}{(r_{\text{crit}}^*)^2}\right]} \tag{8}$$

and is marked by the shaded area. Solutions to the right of this line violate this constraint.

The key design recommendation that emerges from this analysis is that the highest drag is associated with a highly swirling vortex with a small core size. The highest levels of S are found to be just above 1.2, suggesting that the maximum K_c^* limit presented in Eq. (8) is qualitatively in accord with the vortex breakdown criteria mentioned earlier.

3.2 Axisymmetric Streamline Curvature Calculations. The swirl tube drag capability was next modeled with an inviscid, axisymmetric flow solver, MTFLOW [30], within a design space of parametrically defined Burger vortexlike circulation distributions,

---

[3]Note that this is a simple energy constraint only, ignoring the dynamics of vortex breakdown.
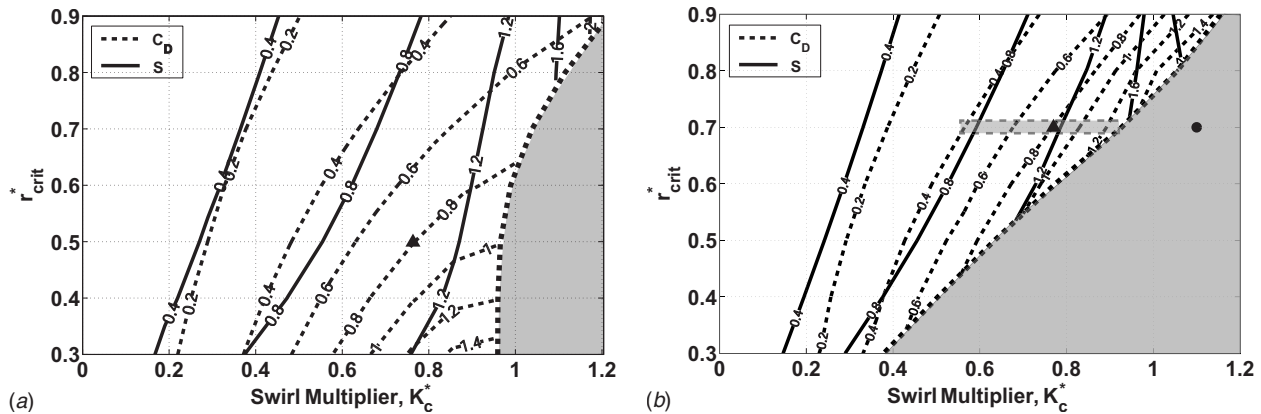
Fig. 4   Isocontours of drag coefficient and swirl number in Burger vortex design space: (a) control volume analysis, and (b) streamline curvature calculation

to produce a family of swirl tube designs defined by their swirl vane exit angles. Designs were chosen to span a range of drag coefficients, both below and above the assumed critical swirl parameter of $S=1.2$, as indicated in Fig. 4(b). The code models the swirl vanes as an actuator disk of finite axial extent inside the nacelle as depicted by the dashed lines in Fig. 2. A loss coefficient of $\bar{\omega}=0.04$ across the actuator disk was assumed. Transition from super- to subcritical wave behavior is demarcated by the shaded area.[4] The pressure coefficient distributions presented earlier in Fig. 2 correspond to cases marked by the triangle (stable) and circle (unstable). The drag coefficient of the stable case is estimated to be 0.8. Furthermore, the exit flow field of this case exhibits (1) a maximum centerline axial velocity of about twice the freestream value, (2) a wakelike axial velocity of about 0.6 times the freestream value at the duct outer radius, (3) a maximum pressure defect of 3.5 dynamic heads, and (4) a maximum exit swirl angle of about 50 deg.

A comparison between the control volume analysis and the streamline curvature computations suggests that the analytical model captures the trends in drag and swirl parameters. For low levels of drag and swirl parameters, e.g., $C_D=0.2$ and $S=0.4$, the isocontours are in good agreement, while at higher values the trends diverge.[5]

3.3   3D Viscous RANS CFD Calculations. The minimum achievable vortex core radius in real swirling flows is limited by viscous effects that are neglected in the streamline curvature computations. A critical radius of $r^*_{\text{crit}}=0.7$ was thus selected to define the circulation distribution for a set of vane setting angles. The choice was based on a compromise between excessive turning at the outer edge near the nozzle shear layer for a large r^*_{crit}, and excessive core vorticity for a small r^*_{crit}, which may compare poorly to a real swirling flow that has large viscous dissipation in the core. This region of the design space is indicated by the shaded horizontal bar in Fig. 4(b).

The output of the streamline curvature code provides the internal and external streamline trajectories in the meridional (axial-radial) plane. Swirling flow streamline exit angles are thus extracted as a function of radius, providing the first step to three-dimensional vane design. Maximum vane exit angles of 34 deg,

41 deg, 47 deg, 53 deg, 57 deg, and 64 deg were selected for various swirl tube designs. Sectional vane design methods were then used to define the three-dimensional vane geometry, on the basis of 20 vanes. High passage solidities in the range of 3 to 4 were chosen to ensure the required flow turning.

Single-passage periodic, fully viscous, RANS CFD calculations, employing the k-ε model, were performed using the commercial code FLUENT for swirl tubes with diameters of 2.16 m to simulate a full-scale device. The CFD calculations include the internal and external flow fields, and contain roughly 1.2 $\times 10^6$ cells. An H-mesh is used to define the vane-to-vane passage region, with streamwise, spanwise, and pitchwise grid densities of 64, 80, and 28 cells, respectively. H-meshes were also used upstream and downstream of the vane, including four points around the leading and trailing edges, respectively. The remainder of the domain used both structured and unstructured meshes with 32 (28+4) circumferential cells. The goals of the CFD experiments were to (1) identify the critical conditions for the onset of the vortex breakdown instability, (2) predict drag coefficients, and (3) describe the exit flow fields to help guide the acoustic analysis.

Figure 5 provides a cut-away view of one-half of the swirl tube internal geometry and presents contours of pressure coefficient, C_p, on the vane and nacelle surfaces, for a swirl vane angle setting of 47 deg. C_p contours are also shown on a plane one-half diameter downstream of the duct exit. The figure demonstrates that a favorable pressure gradient exists within the vanes for this case,
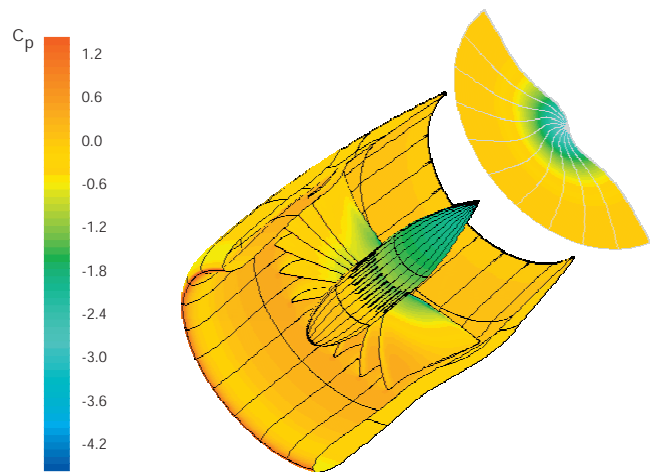

Fig. 5   Favorable streamwise pressure gradient along vanes and maximum pressure defect of 3.5 dynamic heads observed in swirl tube with 47 deg vane exit angle setting
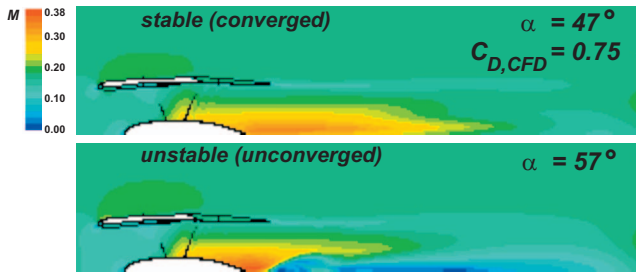
---

[4]Standing wave behavior of the solution indicates this transition (see also Fig. 2).

[5]The circular Burger vortex circulation distribution of Eq. (3) is mapped from radial (r) to streamfunction (ψ) coordinates at the annular actuator disk, under the assumption of uniform axial velocity, i.e., $\psi/\psi_{\text{crit}}=(r^*/r^*_{\text{crit}})^2$. This assumption becomes weaker for high levels of swirl, making the effective core radius slightly smaller than the prescribed value. For example, for the swirl tube designs with r^*_{crit} specified as 0.7, the maximum value of V_θ occurs near $r^*=0.5$. The radial shift of the core is an artifact of the uniform axial velocity assumption, and is the reason that unconverged solutions appear at values of S well below 1.2 for lower values of r^*_c.

Fig. 6 3D CFD calculations: stable exit flow and vortex breakdown, for 47 deg and 57 deg swirl vane angle settings

with a maximum pressure defect on the centerline of $C_p=-3.5$.

The Mach number comparison shown in the axial-radial plane in Fig. 6 demonstrates that vortex breakdown occurs between the swirl vane angle settings of 47 deg and 57 deg, near an exit swirl parameter of 1.2, suggesting this to be a valid indicator of vortex breakdown for this type of flow. Numerically, the breakdown case is unconverged, and manifests itself as a separation bubble on the centerline close to the duct exit (though the flow over the swirl vanes remains attached). The CFD solutions indicate that the length scale of the separation bubble is at the device scale. Overall, RANS CFD computations reveal that a maximum pressure defect near 3.5 dynamic heads is achievable, and that the 47 deg design may be most favorable in terms of drag and acoustics, with an estimated full-scale drag coefficient of 0.75.

4 Experimental Assessment

One-twelfth scale-model aerodynamic and acoustic tests were performed in the MIT Wright Brothers Wind Tunnel (WBWT) and at NASA Langley's Quiet Flow Facility (QFF), respectively, using a 0.179 m diameter model fabricated out of aluminum nacelle parts and interchangeable, one-piece vane cascade inserts made from stereolithography (SLA). Details of the mechanical design are presented in [31]. A picture of the identical swirl tube mounted in both facilities is presented in Fig. 7.

4.1 Aerodynamic Measurements. In the WBWT, the test article was held by a pylon that transmits the aerodynamic forces and moments to a load cell located underneath the tunnel floor. For the stable flow cases, measured drag was also computed by integration of steady velocity profiles obtained through hot-wire anemometry. The primary test objective was to validate the aerodynamic design and to determine the critical swirl angle for the onset of vortex breakdown.

The full test matrix consisting of smoke and oil flow visualization, drag measurements, and steady and unsteady hot-wire measurements in the flow field downstream of the nozzle exit is discussed in [14]. Details of the entire test, including a facility description, are provided in [31], while a selected subset of the results is shown here. Drag coefficients were measured to an estimated experimental error of 0.04. Steady axial and circumferential velocity measurements were made in the vertical plane passing through the swirl tube centerline using hot-wire anemometry by orienting the probe axis perpendicular to the respective directions under the assumption of negligible radial velocity component, invoking simple radial equilibrium. For steady velocity measurements, the average value of single records was computed along radial traverses at axial stations of 0.5, 1.0, 2.0, and 4.0 nozzle diameters downstream of the nozzle exit.

Figure 8 compares CFD predicted and experimentally measured values of dimensionless axial and circumferential velocities, respectively, for a swirl vane angle setting of 34 deg at an axial station 1 diameter downstream of the duct exit plane. Good agreement is achieved, and the size and shape of the viscous core
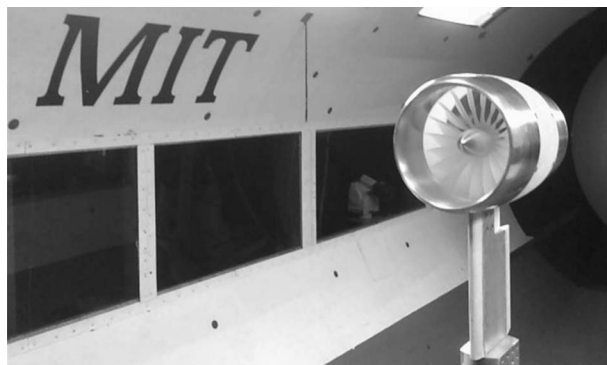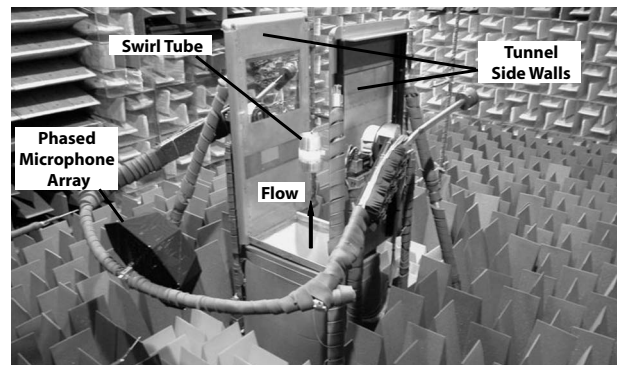
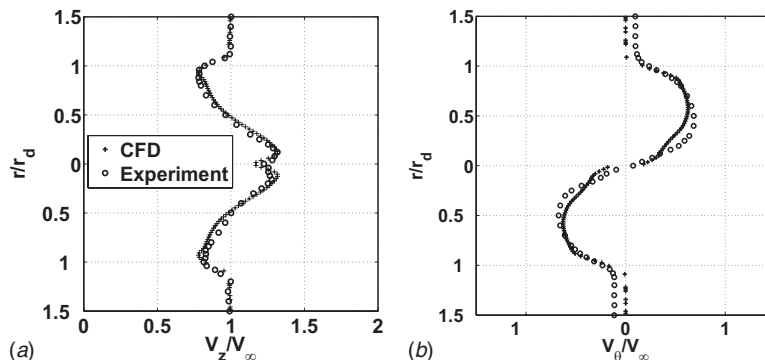**Fig. 7 Swirl tube mounted in MIT Wright Brothers Wind Tunnel (a) and NASA Langley Quiet Flow Facility (b)**

Fig. 8 CFD prediction and measured radial exit profiles of V_x/V_∞ and V_θ/V_∞ at $x/D=1.0$ for 34 deg swirl vane angle setting
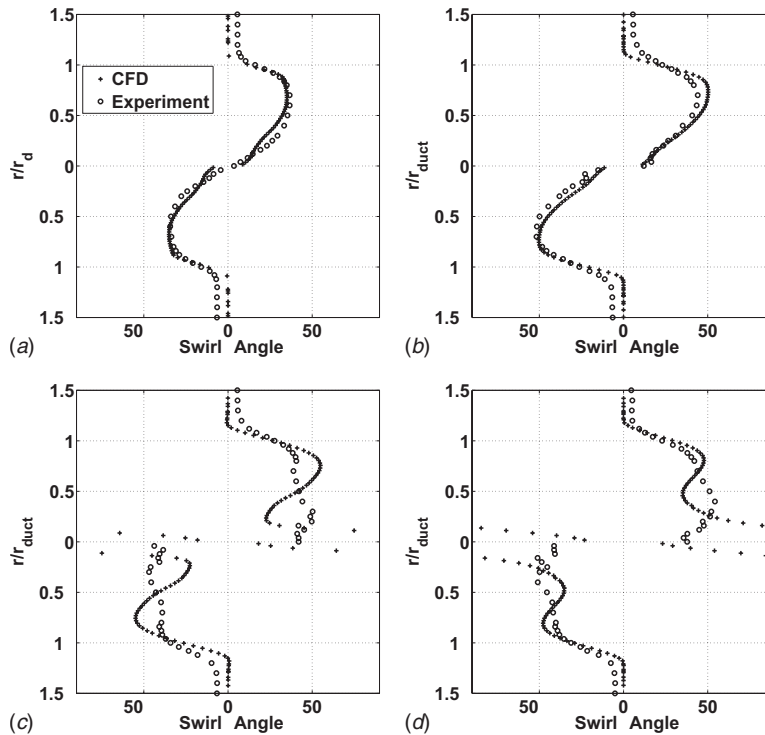
Fig. 9 CFD and measured swirl parameter profile, $S=V_\theta/V_x$, for 34 deg and 47 degree swirl vane angle settings. Discrepancy seen for 57 deg and 64 deg cases is indicative of vortex breakdown. All data are shown for x/D =1.0.

region are well captured. A little overturning, seen in the measured circumferential velocity, appears consistent with slightly higher drag levels presented later in this section.

Figure 9 depicts computed swirl angle distribution, α =$\tan^{-1}(V_\theta/V_x)$, for swirl vane angle settings of 34 deg, 47 deg, 57 deg, and 64 deg, at x/D=1.0. The highest local swirl angle of about 50 deg is achieved in the 47 deg swirl vane angle case, consistent with the critical vortex breakdown criterion of S=1.2 discussed earlier. The discrepancy between CFD and experiment for the 57 deg and 64 deg swirl vane angle cases is indicative of vortex breakdown.

Instantaneous flow visualization images acquired at 30 frames/s for swirl tube vane angle settings of 47 deg and 57 deg are presented in Fig. 10. Smoke was injected via a hand-held heated
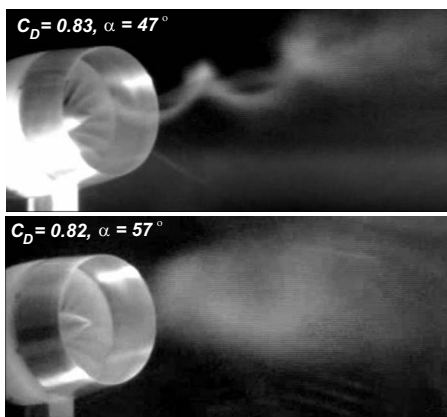

Fig. 10 Instantaneous flow visualization images show stable swirling flow and vortex breakdown, for swirl vane angle settings of 47 deg and 57 deg, respectively

wand that vaporized liquid glycol upstream of the swirl tube. A freestream velocity of 20 m/s was used to minimize turbulent diffusion of the smoke streakline. In the core region the smoke streaklines for the 47 deg swirl vane angle case clearly show a straight line of smoke on the axis of symmetry, surrounded by a tightly coiling helical smoke trail around the core persisting for at least two full wavelengths. This demonstrates that for swirl vane angle settings of 47 deg or lower, the core region is a coherent, tightly swirling flow structure, consistent with the measured swirl angle profiles shown in Fig. 9. The straight line of smoke at the centerline stems from the Burger vortexlike rV_θ distribution selected to generate zero turning at the hub, such that the low momentum fluid in the boundary layers of the centerbody and vanes near the hub exits the swirl vanes axially. The vanes are designed to turn the flow significantly just a short distance away from the hub, such that the helical smoke streakline wraps itself tightly around the core flow.

Bubble-type vortex breakdown [22] is observed for α =57 deg, in good agreement with CFD predictions presented earlier in Fig. 6 and hot-wire measurements from Fig. 9.

Direct swirl tube drag measurements were made using the force and moment balance. Pylon alone drag was first measured and then subtracted from the drag of each of the swirl tube test articles, including an empty nacelle and the case with straight vanes (0 deg of flow turning), used to determine the viscous drag, $C_{D,visc}$. The overall swirl tube experimental drag from the force balance is given by C_D, and the difference between C_D and $C_{D,visc}$ is assumed to equal the experimental pressure drag, $C_{D,press}$.

The experimentally measured drag coefficients[6] are compared against predictions in Table 1 and Fig. 11. All numbers are cor-

---

[6]This represents an average value of drag coefficients taken at various freestream Mach numbers between M=0.06 and M=0.17.

Table 1 Table of measured and CFD computed drag coefficients for model-scale geometry (V.B. indicates vortex breakdown)

Case	Experiment (model-scale)				CFD (corresponding to model-scale)		
	C_D	$C_{D,\text{visc}}$	$C_{D,\text{press}}$	$C_{D,\text{int}}$	C_D	$C_{D,\text{visc}}$	$C_{D,\text{press}}$
Pylon	0.42						
Empty nacelle	0.08						
0 deg	0.14	0.14	0.00				
34 deg	0.52	0.14	0.38	0.48	0.44	0.12	0.32
47 deg	0.83	0.14	0.69	0.81	0.80	0.12	0.68
53 deg	0.85	0.14	0.71	V.B.	0.89	0.12	0.77
57 deg	0.82	0.14	0.68	V.B.	0.94 (V.B.)	0.12	0.82
64 deg	0.76	0.14	0.62	V.B.	0.98 (V.B.)	0.10	0.88

rected to model-scale geometry using a Reynolds number correction for the viscous drag component based on turbulent flat plate skin friction coefficient [32]

$$C_f \propto \text{Re}^{1/5} \qquad (9)$$

Measured drag coefficients are found to be higher than the predictions for stable flow vane setting angles (less than 47 deg). This is suggested to be due to small differences in flow turning observed in the steady velocity profiles taken with hot-wire anemometry (see [14]). A maximum stable flow model-scale drag coefficient of 0.83, comparable to bluff body drag, is measured for the 47 deg swirl vane angle case. A full-scale Reynolds number correction suggests a drag coefficient of 0.78 for a vane outer diameter of 2.16 m. Maximum drag coefficient occurs near the flow regime change from stable swirling flow to vortex breakdown.

For the stable flow cases with swirl vane angle settings of 34 deg and 47 deg, the total drag coefficient was also independently estimated by integration of the hot-wire axial and circumferential velocity profiles at $x/D = 1.0$, assuming the flow satisfied simple radial equilibrium (for details, see [14]). It is given in the table by $C_{D,\text{int}}$. The drag estimate from measured velocity profile integration of the stable cases is consistent to within 0.04 of the drag coefficient values measured on the force and moment balance. The overall CFD drag coefficient is calculated by force integration over the swirl tube vane, nacelle, and centerbody surfaces. The total drag is made up of viscous and pressure components, $C_{D,\text{visc}}$ and $C_{D,\text{press}}$, respectively, obtained from shear and normal force integrations over these surfaces.

4.2 Acoustic Measurements. The NASA Langley QFF is a state of the art anechoic free jet wind tunnel facility used in the past for seminal measurements of self-noise from airfoils, flaps, slats, and simulated landing gear components [33–36]. The facility test chamber, shown in Fig. 7, has a vertical 0.61×0.91 m^2 free jet nozzle housed within a $9.1 \times 6.1 \times 7.6$ m^3 anechoic cham-
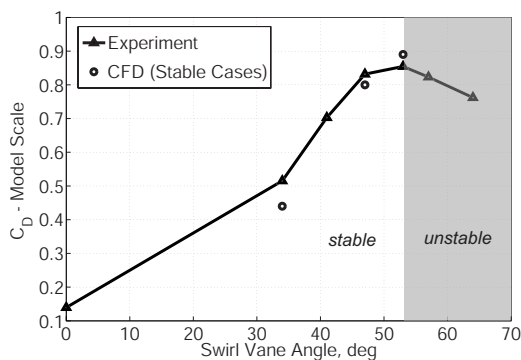

Fig. 11 Experimentally measured drag coefficient versus swirl angle (model-scale). 3D viscous CFD prediction for converged cases shown for comparison.

ber. Sound absorbing foam wedges line all sides of the chamber to prevent reflections. Additional details of the facility can be found in [37].

Acoustic pressure time-histories were acquired using six fixed-pole microphones and a medium aperture directional array (MADA) consisting of 41 microphones covered with a cloth wind screen. The array is mounted on a boom and can be rotated to forward, aft, and side directivity angles [35]. The radial distance from the test article center to the center of the array was 1.524 m. The results are shown for the MADA at the side directivity position. The six pole microphones were located at a radial distance of 1.995 m at forward, aft, and side directivity locations relative to the test article on the near and far sides of the tunnel. The results from pole microphones are not presented here. For additional information on the swirl tube acoustic tests, the reader is referred to [23].

The working hypotheses are that stable, highly swirling flows can produce high levels of drag for relatively low levels of noise, and that the primary swirl tube noise sources consist of turbulence mixing noise and scattering of turbulent structures near edges. Figure 12 presents the full-scale drag coefficient and A-weighted, overall sound pressure level (OASPL)[7] at the International Civil Aviation Organization (ICAO) approach certification location[8] as a function of swirl vane angle. The acoustic energy is scaled up as the square of the diameter and the inverse square of the observer distance. The plot demonstrates that the full-scale drag coefficient of 0.78 found in the stable 47 deg swirl vane case also corresponds to an A-weighted OASPL of 44 dBA, about 20 dBA quieter than a well-populated urban area in the vicinity of an airport, and comparable with noise levels in a quiet library. All of the stable flow cases have similar OASPLs, within an estimated error of ± 2 dBA [31], suggesting this noise-to-drag characteristic is different from the one-to-one relationship of conventional drag devices such as flaps, slats, spoilers, and struts (e.g., landing gear).

Figure 13 compares the narrowband (17.44 Hz bandwidth) autospectra of the cases with swirl vane angle settings of 47 deg and 57 deg as measured by a single MADA microphone. Empty tunnel background noise with Mach 0.17 flow (green) indicates that the data are acquired with good signal-to-noise ratio for frequencies higher than 1 kHz. Both swirl tube spectra are broadband in nature, with no strong tones present. Vortex breakdown near the duct exit yields a white-noise-like spectrum with a 15 dB increase in SPL over the entire frequency range.

An advanced phased array-based source diagnostic technique developed by Brooks and Humphreys [38] was employed to dissect the swirl tube noise sources. The deconvolution approach for the mapping of sources (DAMAS) output provides a spatial source mapping of the mean square value of the fluctuating pressure, $\langle p'^2 \rangle$, in decibel, on a volumetric basis, at each grid point for

---

[7]Taken from a single array microphone.
[8]Directly 105 m overhead, assuming an aircraft on a 3 deg glideslope 2000 m from touchdown.
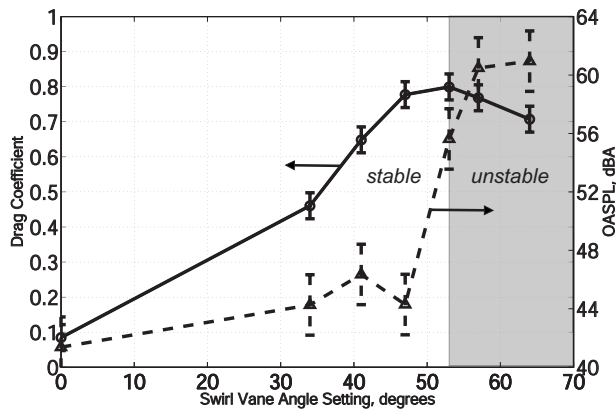
Fig. 12 Full-scale noise versus drag versus swirl angle relationship shows high-drag and low-noise capabilities for swirl vane angle setting of 47 deg

each one-third octave band frequency. The total sound pressure level in any given frequency band is thus simply the $\langle p'^2 \rangle$ summation of the values at all of the grid points. The DAMAS procedure enables reconstruction of an entire autospectrum, as well as selective spectra from spatial source regions to isolate different noise source mechanisms.

Figures 14 and 15 present source maps and one-third octave integrated spectra constructed from the DAMAS array postprocessing program for the 47 deg and 57 deg swirl vane cases, respectively, at a M=0.17 sideline angle (−90 deg) test point. The three integration zones used to dissect the acoustic signature are also shown in Fig. 14(e). Flow is from bottom to top. Zone 1 is the aft region, enclosing the swirling flow field as well as the nacelle exit. Zone 2 is the forward region, enclosing the nacelle inlet. Zone 3 is the pylon region, enclosing the entire pylon on which the swirl tube is mounted in the facility.

The computed DAMAS outputs show the localized spectra of the aft, fore, and pylon regions as circular, triangular, and square symbols, respectively, and the overall noise spectra as diamonds. Good agreement is found between the overall DAMAS computed noise spectra, and autospectra from two individual array microphones, presented as solid cyan and magenta lines. Background noise is also provided in green, for reference. In the bottom two rows of each figure, DAMAS source maps for the 2.5 kHz, 16 kHz, and 31.5 kHz third-octave bands indicate regions of high source intensity.

It should be noted that each DAMAS source map presented here has its own scaling to illustrate the source location more clearly. The integrated source spectra for the 47 deg swirl vane angle setting in Fig. 14 indicate a clear aft zone source dominance
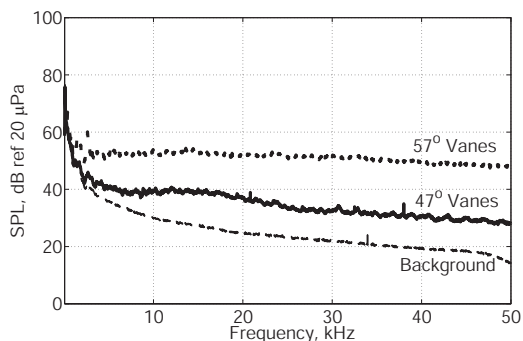

Fig. 13 Narrowband (17.44 Hz) spectra for 47 deg versus 57 deg swirl vane angle. Background noise shows good signal-to-noise ratio. Tunnel Mach number is 0.17 in all cases.

at frequencies above 3 kHz. Below this frequency both aft and pylon zones contribute to the noise signature. The DAMAS source maps indicate a volume source downstream of the duct trailing edge at all three selected frequencies. In the 2.5 kHz third-octave band there is a significant source activity near the pylon trailing edge, while in the 16 kHz and 31.5 kHz third-octave bands there is an activity near the duct exit. The activity both in the outflow region of the swirling flow and near the duct and pylon trailing edges suggests the presence of both quadruple- and scattering/dipole-type sources.

By contrast the 57 deg vane angle setting case with vortex breakdown displays an aft dominant behavior at all selected frequencies, as shown by the integrated spectra and the source maps of Fig. 15. It is suggested that the burst vortex generates its own noise and is likely to affect the trailing edge noise of the pressure-driven flow exiting the duct. The unsteadiness may provide a mechanism to amplify the scattering and/or dipolelike edge noise sources, in addition to creating its own quadruplelike self-noise. In addition, the pylon trailing edge source is independent of the swirling flow dynamics, and is hence present in both the stable and the vortex breakdown case. As shown by the 2.5 kHz source map, however, the magnitude of the vortex breakdown noise source is loud enough to mask the distributed pylon trailing edge source seen in the 47 deg swirl vane case of the previous figure.

In summary, at the scale needed for commercial aircraft operation, and at the ICAO approach certification point, a RAM pressure-driven swirl tube can be designed to have a relatively quiet A-weighted OASPL of about 44 dBA, well below the background noise of a well-populated area. DAMAS source maps suggest that the noise from high-drag generating, stable swirling flow cases is dominated by scattering/dipole sources at the duct edge and quadruple sources in the swirling outflow. Vortex breakdown noise is dominated by a concentrated source near the duct exit. Vortex breakdown introduces a dramatic increase in noise, with sources concentrated at the duct exit (and edges). At high frequencies, the vortex breakdown spectrum appears similar to white noise and is about 15 dB louder than a highly swirling, stable case.

5 Summary

A novel air-brake concept called a swirl tube is introduced for next-generation, low-noise civil aircraft, as a possible enabler to fly a slower and steeper approach trajectory in clean airframe configuration with the goal to reduce aircraft source noise and noise propagation to the ground. The swirl tube concept was assessed from first principles using a control volume analysis. A family of designs was defined using a streamline curvature method parametric study to explore the design space. The limiting phenomenon for stable swirling flow was found to be vortex breakdown, and a detailed aerodynamic design was carried out on a selected set of swirl tube geometries using three-dimensional RANS calculations.

A model-scale set of swirl tubes with various vane angle settings was experimentally assessed through aerodynamic and acoustic wind tunnel tests. The results of these tests demonstrate that swirling flows can generate drag coefficients of about 0.8 at low-noise levels. In addition, it was shown that vortex breakdown sets the swirling flow stability limit, the maximum drag generation capability, and the low-noise threshold.

6 Outlook

Two types of swirl tube configurations, a fan-driven or pumped concept, and a ram pressure-driven concept, are suggested. Extensive design and validation of the ram pressure-driven swirl tube represented the simplest means to demonstrate the concept of a quiet drag device that uses swirling outflow. In practice, the propulsion system integrated or fan-driven configuration represents the more likely arrangement, due to weight and performance
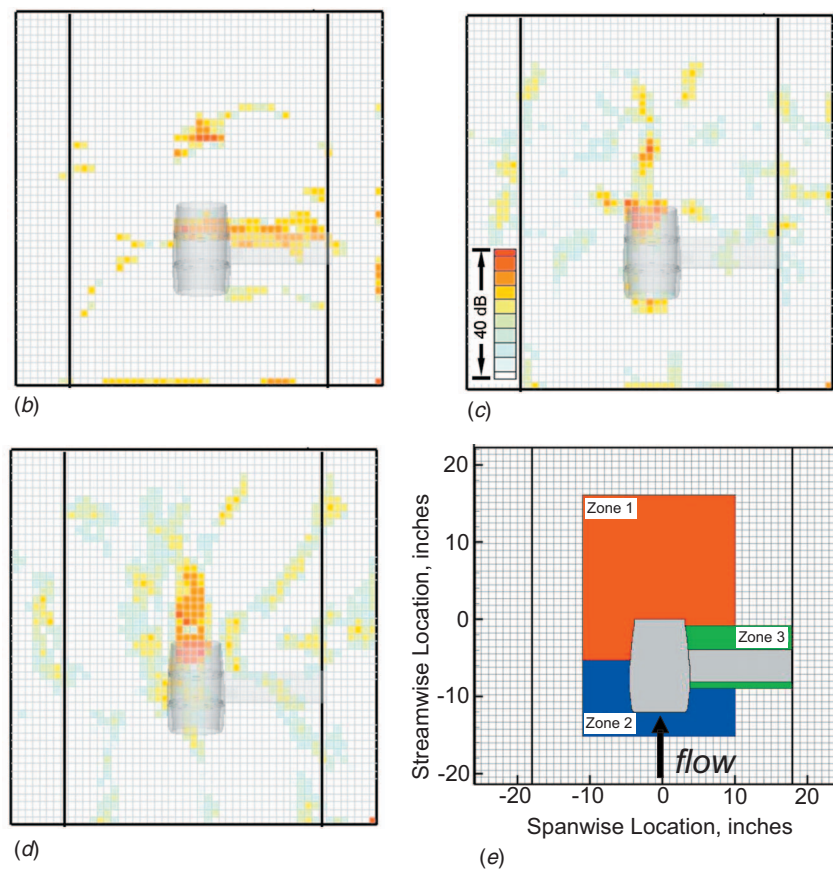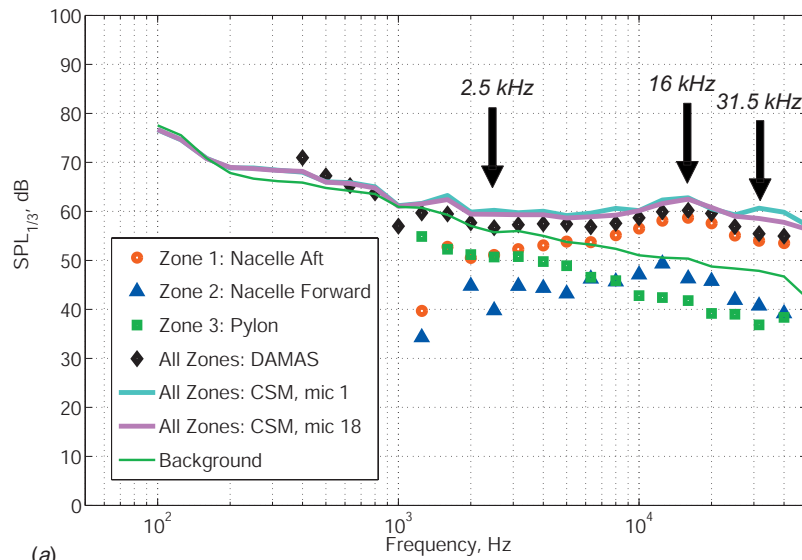
Fig. 14 DAMAS zone-integrated spectra and source maps, 47 deg swirl vane angle case, M=0.17, $\theta=-90$ deg. Swirl tube shown in gray in source maps.

concerns. Fan-driven configurations may be realizable through variable OGVs or deployable swirl vanes located in the bypass or mixing duct of an ultrahigh bypass ratio turbofan propulsion system. These configurations have the benefit of integrating into the existing propulsion system but have the challenge of interacting with a pumping (fan) stage located upstream. Integration challenges include fan stage operability due to the resistance applied by the vanes, and mitigation of blade row interaction noise. The deployable vanes may also have the additional benefit of actuating

to a fully closed position, in order to serve as blocker doors within a thrust reverser system, as depicted in Fig. 16. This would potentially save weight when compared with stand-alone quiet drag and thrust reverse systems, and also enable more rapid thrust reverser deployment on landing.

Future work needs to focus on developing a rigorous understanding of the aerodynamics and acoustics of the fan-driven swirl tube concept. A preliminary analysis of this concept, including quiet drag requirements, is presented in [14,15], and suggests that
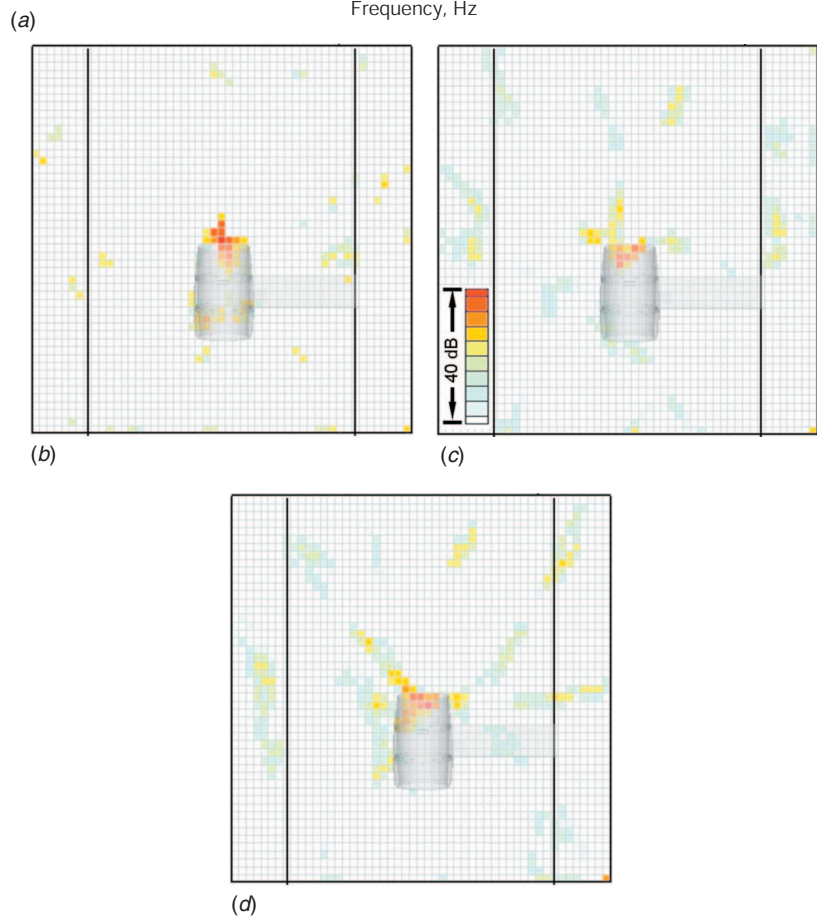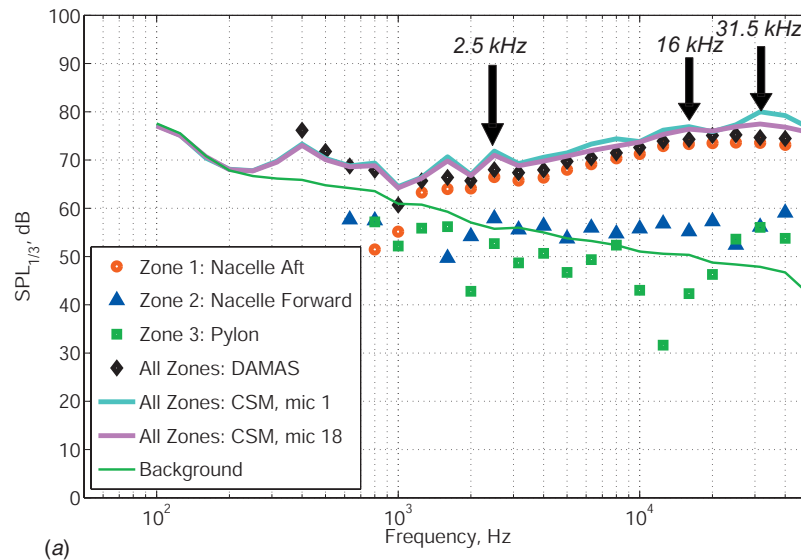
Fig. 15 DAMAS zone-integrated spectra and source maps, 57 deg swirl vane angle case, M=0.17, θ=−90 deg. Swirl tube shown in gray in source maps.
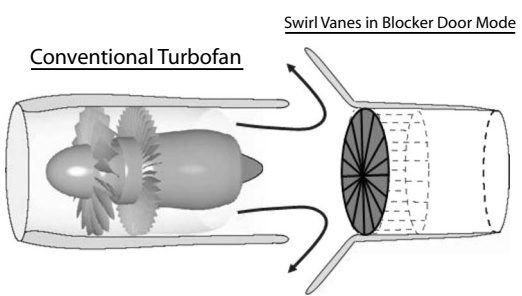

Fig. 16 Pumped swirl tube configuration in thrust reverser blocker door mode

pumping is beneficial in terms of drag, but may be detrimental in terms of noise, due to the increase in ingested mass flow and increased exhaust velocities. Preliminary acoustic measurements of the ram air-driven swirl tube with upstream flow distortion such as circumferentially periodic wakes also suggest that the noise signature may be robust to fan stage generated turbulence [31]. Experimental assessment of this configuration for both drag and noise is recommended to determine if a significant system level noise reduction is possible. Implementation challenges that warrant further study include fan operability and capability to integrate swirl vanes into a thrust reverser system.

Acknowledgment

Nomenclature

Roman

A = area
C_D = drag coefficient
C_f = skin friction coefficient
C_p = pressure coefficient
D = diameter
F = force, drag
K = circulation
M = Mach number
p = pressure
r = radial direction, distance
Re = Reynolds number
S = swirl parameter
V = velocity
x = axial direction

Greek

α = swirl angle
θ = circumferential direction, microphone polar angle
ρ = density
ψ = streamfunction
$\bar{\omega}$ = loss coefficient

Subscripts/Superscripts

$(\ )_c$ = critical
$(\ )_{crit}$ = critical
$(\ )_d$ = discharge or nozzle exhaust
$(\ )_f$ = actuator disk face
$(\ )_{int}$ = integrated value
$(\ )_{press}$ = pressure component
$(\ )_{visc}$ = viscous component
$(\ )_\infty$ = freestream
$(\ )^*$ = nondimensional
$(\ )'$ = fluctuating component

References

[1] Lilley, G. M., 2001, "The Prediction of Airframe Noise and Comparison With Experiment," J. Sound Vib., **239**, pp. 849–859.
[2] Smith, M. J. T., 1989, *Aircraft Noise*, Cambridge University Press, Cambridge.
[3] Howe, M. S., 1978, "A Review of the Theory of Trailing Edge Noise," J. Sound Vib., **61**, pp. 437–465.
[4] Lockard, D. P., and Lilley, G. M., 2004, "The Airframe Noise Reduction Challenge," Reference Publication 213013, NASA, Hampton, VA.
[5] Clarke, J. B., Ho, N. T., Ren, L., Brown, J. A., Elmer, K. R., Tong, K., and Wat, J. K., 2004, "Continuous Descent Approach: Design and Flight Test for Louisville International Airport," J. Aircr., **43**, pp. 1054–1066.
[6] Reynolds, T. G., Ren, L., Clarke, J. B., Burke, A. S., and Green, M., 2005, "History, Development and Analysis of Noise Abatement Arrival Procedures for UK Airports," AIAA Fifth Aviation, Technology, Integration and Operations Conference, Arlington, VA, Sept. 26–28, Paper No. AIAA-2005-7395.
[7] Lutz, T., and Wieser, T., 2006, "Heading for the City: A318 Steep Approach Development," International Federation of Airline Pilots' Associations, I.F.-.A.L.P.A. News, Apr.
[8] Diedrich, A., Hileman, J., Tan, D., Wilcox, K., and Spakovszky, Z., 2006, "Multidisciplinary Design and Optimization of the "Silent" Aircraft," 44th AIAA Aerospace Sciences Meeting and Exhibit, Reno, NV, Jan. 9–12, Paper No. AIAA-2006-1323.
[9] Hileman, J., Spakovszky, Z., Drela, M., and Sargeant, M., 2006, "Aerodynamic and Aeroacoustic Three-Dimensional Design for a "Silent" Aircraft," 44th AIAA Aerospace Sciences Meeting and Exhibit, Reno, NV, Jan. 9–12, Paper No. AIAA-2006-241.
[10] Manneville, A., Pilczer, D., and Spakovszky, Z. S., 2006, "Preliminary Evaluation of Noise Reduction Approaches for a Functionally Silent Aircraft," J. Aircr., **43**, pp. 736–740.
[11] Manneville, A., Pilczer, D., and Spakovszky, Z., 2004, "Noise Reduction Assessments and Preliminary Design Implications for a Functionally-Silent Aircraft," Tenth AIAA/CEAS Aeroacoustics Conference, Manchester, UK, May 10–12, Paper No. AIAA-2004-2925.
[12] Agarwal, A., and Dowling, A. P., 2005, "The Calculation of Acoustic Shielding of Engine Noise by the Silent Aircraft Airframe," 11th AIAA/CEAS Aeroacoustics Conference, Monterey, California, USA, May 23–25, Paper No. AIAA-2005-2996.
[13] Hall, C. A., and Crichton, D., 2006, "Engine Design Studies for a Silent Aircraft," ASME Paper No. GT2006-90559.
[14] Shah, P. N., 2006, "Novel Turbomachinery Concepts for Highly Integrated Airframe/Propulsion Systems," Ph.D. thesis, MIT, Cambridge, MA.
[15] Shah, P. N., Mobed, D., and Spakovszky, Z. S., 2007, "Engine Air-Brakes for Quiet Air Transport," 45th AIAA Aerospace Sciences Meeting and Exhibit, Reno, NV, Jan. 8–11, Paper No. AIAA-2007-1033.
[16] Mager, A., 1974, "Steady, Incompressible, Swirling Jets and Wakes," AIAA J., **12**, pp. 1540–1547.
[17] Loiseleux, T., Delbende, I., and Huerre, P., 2000, "Absolute and Convective Instabilities of a Swirling Jet/Wake Shear Layer," Phys. Fluids, **12**, pp. 375–380.
[18] Schwartz, I., 1973, "Swirling Flow Jet Noise Suppressors for Aircraft Engines," AIAA Aeroacoustics Conference, Seattle, WA, Oct. 15–17, Paper No. AIAA-1973-1003.
[19] Lu, H., Ramsay, J., and Miller, D., 1977, "Noise From Swirling Exhaust Jets," AIAA J., **15**, pp. 642–646.
[20] Delery, J. M., 1994, "Aspects of Vortex Breakdown," Prog. Aerosp. Sci., **30**, pp. 1–59.
[21] Hall, M. G., 1972, "Vortex Breakdown," Annu. Rev. Fluid Mech., **4**, pp. 195–218.
[22] Leibovich, S., 1978, "The Structure of Vortex Breakdown," Annu. Rev. Fluid Mech., **10**, pp. 221–246.
[23] Shah, P. N., Mobed, D., and Spakovszky, Z. S., 2007, "Aero-Acoustics of Drag Generating Swirling Exhaust Flows," presented at The 28th AIAA/CEAS Aeroacoustics Conference, Rome, Italy, May 21–23.
[24] Squire, H. B., 1960, "Analysis of the 'Vortex Breakdown' Phenomenon," Imperial College, Aeronautics Department, Report No. 102.
[25] Brooke Benjamin-Zword, T., 1962, "Theory of the Vortex Breakdown Phenomenon," J. Fluid Mech., **14**, pp. 593–629.
[26] Darmofal, D. L., Khan, R., Greitzer, E. M., and Tan, C. S., 2003, "Vortex Core Behavior in Confined and Unconfined Geometries: A Quasi-One-Dimensional Model," J. Fluid Mech., **449**, pp. 61–84.
[27] Greitzer, E. M., Tan, C. S., and Graf, M. B., 2004, *Internal Flow Concepts and Applications*, Cambridge University Press, Cambridge.
[28] Bearman, P. W., 1967, "The Effect of Base Bleed on the Flow Behind a Two-Dimensional Model With a Blunt Trailing Edge," Aeronaut. Q., **18**, pp. 207–224.
[29] Sevilla, A., and Martínez-Bazán, C., 2004, "Vortex Shedding in High Reynolds Number Axisymmetric Bluff-Body Wakes: Local Linear Instability and Global Bleed Control," Phys. Fluids, **16**, pp. 3460–3469.
[30] Drela, M., 1997, "A User's Guide to MTFLOW 1.2—Multi-Passage Throughflow Design/Analysis Program," Nov.
[31] Mobed, D., 2007, "Experimental Aero-Acoustic Assessment of Swirling Flows for Drag Applications," MS thesis, MIT, Cambridge, MA.
[32] Schlichting, A. H., 1987, *Boundary Layer Theory*, McGraw-Hill, New York.
[33] Brooks, T. F., 1989, "Airfoil Self-Noise and Prediction," Reference Publication 1218, NASA, Hampton, VA.
[34] Mendoza, J. M., Brooks, T. F., and Humphreys, W. M., Jr., 2002, "Aeroacoustic Measurements of a Wing-Slat Model," Eighth AIAA/CEAS Aeroacoustics Conference, Breckenridge, CO, Jun. 17–19, Paper No. AIAA-2002-2604.
[35] Brooks, T. F., and Humphreys, W. M., Jr., 2003, "Flap-Edge Aeroacoustic Measurements and Prediction," J. Sound Vib., **261**, pp. 31–74.
[36] Hutcheson, F. V., and Brooks, T. F., 2002, "Noise Radiation From Single and Multiple Rod Configurations," 12th AIAA/CEAS Aeroacoustics Conference, Cambridge, MA, May 8–10, Paper No. AIAA-2006-2629.
[37] Hubbard, H. H., and Manning, J. C., 1983, "Aeroacoustic Research Facilities at NASA Langley Research Center: Description and Operational Characteristics," Technical Memorandum No. TM-84585, NASA, Hampton, VA.
[38] Brooks, T. F., and Humphreys, W. M., Jr., 2006, "A Deconvolution Approach for the Mapping of Acoustic Sources (DAMAS) Determined From Phased Microphone Arrays," J. Sound Vib., **294**, pp. 856–879.